Journal of Fluids and Structures (2002) **16**(5), 667–683
doi:10.1006/jfls.439 available online at http://www.idealibrary.com on IDEAL®

MODELLING THE UNSTEADY AXIAL FORCES ON A FINITE-LENGTH CIRCULAR CYLINDER IN CROSS-FLOW

D.E. Capone[a] and G.C. Lauchle[b]

[a] *Applied Research Laboratory, Pennsylvania State University, P. O. Box 30
State College, PA 16804, USA*
[b] *Graduate Program in Acoustics and Applied Research Laboratory, Pennsylvania State
University, P. O. Box 30 State College, PA 16804, USA*

(Received 26 July 2000; and in final form 13 September 2001)

A semi-empirical model for unsteady axial forces is developed to predict the spectral features of the force generated by the flow over the end-caps on a finite-length, right circular cylinder in cross-flow. In general, the model consists of two parts: the spatial variation of r.m.s. wall pressure on the cylinder end-caps, and the correlation lengths and areas, which describe the spatial extent of the correlation of the unsteady wall pressures. Experiments were conducted in a low-noise wind tunnel as a function of cylinder diameter Reynolds number ($19\,200 < \mathrm{Re} < 32\,000$) and the Strouhal number ($0{\cdot}05 < \mathrm{St} < 3{\cdot}33$) to measure the statistics of the unsteady wall pressures on a model cylinder. These results are incorporated into the theoretical models, and prediction of the spectral characteristics of the axial force are made. The r.m.s. wall pressures on the end-caps are found to have the largest amplitude at circumferential locations (from the forward stagnation point) in the 90–120° range. The high levels at these locations are attributed to reattachment of the separated flow over the end-cap. The radial and circumferential correlation areas have a maximum value at $\mathrm{St} = 0{\cdot}21$. Due to the 3-D flow over the end-caps, the radial correlation areas are found to depend on the circumferential measurement reference location, and the circumferential correlation lengths are found to depend on the radial measurement location. The unsteady axial force predictions using the model show a very broad spectral character.

1. INTRODUCTION

Suspended underwater acoustic sensors are used in numerous applications for the measurement and localization of underwater sound sources. The performance of these sensors is degraded by the presence of various background noise sources such as: oceanic ambient noise, electronic noise, mechanical suspension-induced noise, and flow noise. Flow noise results from the sensor being located in an environment where fluid flows over the body of the sensor. In the case of sensors configured as bluff bodies, the fluid is disturbed as it passes over the sensor, resulting in turbulence on the surface and in the wake of the body. The turbulence produces time-dependent pressure fluctuations on the surface of the sensor, which result in forces acting on the sensor. Pressure, pressure gradient, and acoustic velocity hydrophones, in addition to acoustic intensity probes, respond to these unsteady body forces, resulting in a spurious signal known as flow noise. The problem is particularly important for inertial sensors; the outputs of which are proportional to acoustic particle velocity or acceleration. One common shape used for underwater acoustic sensors is that of a finite-length right circular cylinder. Finger *et al.*

0889-9746/02/050667 + 17 $35.00/0

(1979) and McEachern & Lauchle (1995) have shown that the unsteady forces on such finite-length cylinders can result in flow-induced self-noise being the major component of the transducer output signal.

Significant research has been performed on the measurement and prediction of unsteady lift and drag on 2-D, or "infinite-length", cylinders in cross-flow. Ribeiro (1992) provided a comprehensive review of the fluctuating lift and spanwise correlation characteristics determined for 2-D cylinders. Considerably less work has been done on the unsteady lift and drag on finite-length, or 3-D cylinders, due to the complexity of the problem and due to the limited application of the results. To date, no data are available on the unsteady axial forces generated on finite-length cylinders in cross-flow.

The work of McEachern (1993) and McEachern & Lauchle (1995) quantified the unsteady lift and drag on finite-length, cylindrical-shaped hydrophones of various aspect ratios and end-cap corner radii. They found that the flow-induced noise on a pressure gradient, or acoustic particle velocity hydrophone decreases as the aspect ratio increases. They also found an optimum corner radius for minimum flow noise output, and that the unsteady force spectra are broadband. Considerable energy at frequencies above the predicted vortex-shedding frequency was observed. This observation is consistent with those of Keefe (1961), who noted that the flow over the cylinder body near open clearance holes in the tunnel wall caused a decorrelation of the vortex-shedding process behind the cylinder, resulting in wake energy which is more broadband in nature. Farivar (1981) measured fluctuating pressures and forces on a cylinder with one end free and the other end mounted to the wall of a wind tunnel. The length-to-diameter ratio (L/D) ranged from 2·78 to 12·5 at a Reynolds number based on free-stream velocity and cylinder diameter of $7{\cdot}0 \times 10^4$. Definite vortex-shedding frequencies are present on the signals of the pressure sensors for $L/D > 7{\cdot}5$, but for smaller aspect ratios, no discrete shedding frequency was detected.

Baban et al. (1989) measured unsteady forces on both a 2-D and a 3-D cylinder with one free end. Flow visualization showed an unsteady flow reversal region behind the 3-D cylinder. The size of this reversed flow region is approximately two cylinder diameters in streamwise length, and of width comparable to the span (L) of the cylinder. The presence of the separated flow over the end of the cylinder and the large unsteady recirculation zone inhibits the formation of coherent vortices along the span of the cylinder. The fluctuating local drag for the 3-D case was found to be larger than the fluctuating local lift measured near the free end of the cylinder.

Due to the complexity of the flow field for the given cylinder orientation, no analytical model for the unsteady axial force generated on a finite-length circular cylinder in either steady or unsteady flow exists. The objective of this work is to develop semi-empirical models for the statistics of the end-cap surface pressure field, in order to predict the spectral features of the unsteady axial force on finite-length, right circular cylinders in uniform, steady cross-flow. It represents an extension of our previous work (Capone & Lauchle 2000) that considered the unsteady lift and drag forces. The models together can be used for the prediction of the statistical features of the flow noise signal of inertial acoustic sensors of this configuration.

2. THEORY

The coordinate system for the circular cylinder is shown in Figure 1. For a single end-cap, the unsteady axial force is given by

$$f_z(t) = \int_0^a \int_0^{2\pi} p(r, \theta, t) r \, \mathrm{d}r \, \mathrm{d}\theta, \tag{1}$$

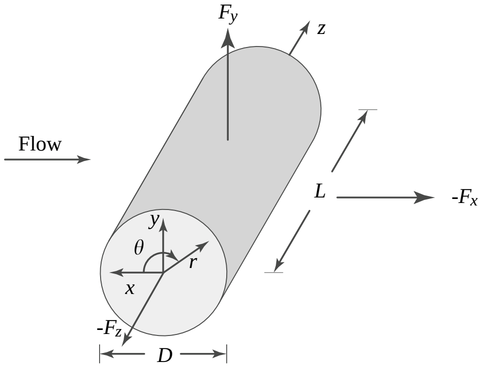

Figure 1. Coordinate system for the right circular cylinder in cross-flow.

where $p(r, \theta, t)$ is the unsteady pressure on the surface of the end-cap, and a is the radius of the end-cap. Axially oriented unsteady wall shear stresses on the cylindrical portion of the body are assumed negligible in this description of $f_z(t)$. The autocorrelation of the unsteady axial force, using the notation of Bendat & Piersol (2000) for stationary signals, may be represented as

$$R_{f_z f_z}(\tau) = \mathrm{E}[f_z(t) f_z(t+\tau)], \tag{2}$$

where the variable τ is the time delay between any two signals and E[ ] represents the expected value which is an ensemble average over N records. Substitution of equation (1) into equation (2) yields

$$R_{f_z f_z}(\tau) = \int_0^a \int_0^a \int_0^{2\pi} \int_0^{2\pi} \mathrm{E}\left[p(r, \theta, t) p(r', \theta', t+\tau)\right] r \,\mathrm{d}r\, r' \,\mathrm{d}r' \,\mathrm{d}\theta \,\mathrm{d}\theta'. \tag{3}$$

Twice the temporal Fourier cosine transform of equation (3) results in the one-sided autospectrum for the unsteady axial force

$$G_{zz}(f) = \int_0^a \int_0^{2\pi} \int_0^a \int_0^{2\pi} \Gamma(f, r, r', \theta, \theta') r \,\mathrm{d}r \,\mathrm{d}\theta\, r' \,\mathrm{d}r' \,\mathrm{d}\theta', \quad f \geq 0. \tag{4}$$

Here, $\Gamma(f, r, r', \theta, \theta')$ is the cross-spectral density of the wall-pressure fluctuations on the end-cap.

It can be seen from equation (4) that the spectrum of the unsteady axial force on the cylinder can be calculated if the wall-pressure cross-spectra among all points on the end-cap of the cylinder are known. In this research, we consider equation (4) with a model of the cross-spectral densities and corresponding correlation areas. The model for the unsteady axial force is developed in a manner that permits calculations of the unsteady forces on similar cylinders in cross-flow, with knowledge of only a limited number of experimental measurements.

2.1. MODEL FOR THE UNSTEADY AXIAL FORCES

A frequency-dependent correlation area (Crighton et al. 1992) for the unsteady axial force is defined as

$$S_{ce}(f, r, \theta) \equiv \frac{\int_0^a \int_0^{2\pi} \Gamma(f, r, \theta, r', \theta') r' \,\mathrm{d}r'\, \theta' \,\mathrm{d}\theta'}{\Gamma(f, r, \theta)}, \tag{5}$$

where $\Gamma(f, r, \theta)$ represents the one-sided autospectrum of the wall-pressure fluctuations at location r and θ. The larger the region over which the pressures are correlated, the larger the value for the correlation area, and hence the larger will be the unsteady axial force on the cylinder.

For convenience, we will assume

$$S_{ce}(f, r, \theta) = \Lambda_r(f, r, \theta)\Lambda_\theta(f, r, \theta), \tag{6}$$

where $\Lambda_r(f, r, \theta)$ and $\Lambda_\theta(f, r, \theta)$ are the radial and circumferential scales, respectively. Dependence on all variables must be retained because of the inhomogeneity of the wall-pressure field. Before defining these scales, a change of variables will be made in the cross-spectral density representation used in equation (4). In particular, let $\theta' = \Delta\theta + \theta$ and $r' = \Delta r + r$. The new variables allow for the measurement of cross-spectral densities as functions of both reference measurement location, and separation distance. With the specified changes in variables, and the form of equation (6), the end-cap radial correlation scale, is actually a correlation area defined by

$$\Lambda_r(f, r, \theta) = \int_{-r}^{a-r} \frac{\Gamma(f, r, \Delta r)}{\Gamma(f, r, \theta)}(r + \Delta r)\, \mathrm{d}\Delta r. \tag{8}$$

The circumferential correlation scale is in radians according to

$$\Lambda_\theta(f, r, \theta) = \int_{-\theta}^{2\pi-\theta} \frac{\Gamma(f, \theta, \Delta\theta)}{\Gamma(f, r, \theta)}\, \mathrm{d}\Delta\theta. \tag{9}$$

The last step in the modelling of the unsteady axial forces, is the introduction of a simplified representation for the surface pressure spectrum on the cylinder end-cap. Let

$$\Gamma(f, r, \theta) = G_{p_r p_r}(f, r_r, \theta_r)B(r, \theta), \tag{10}$$

where $G_{p_r p_r}(f, r_r, \theta_r)$ is a reference autospectral density of the wall pressure, $\mathrm{p_r}$, measured at a specified reference location (r_r, θ_r). The function $B(r, \theta)$ is an empirically determined function describing the dependence of the mean-square value of the unsteady wall pressure on measurement location. For this investigation, $G_{p_r p_r}$ is taken at the center of the end-cap, (r_r, θ_r) = (0,0).

Nondimensionalizing length variables on the end-cap radius, and substituting equations (10), (9) and (8) into equation (4) results in the final form for the autospectral density for the unsteady axial force on the 3-D cylinder in cross-flow:

$$G_{zz}(f) = G_{p_r p_r}(f, r_r/a, \theta_r)a^4 \int_0^1 \int_0^{2\pi} \Lambda_r(f, r/a, \theta)\Lambda_\theta(f, r/a, \theta)B(r/a, \theta)\left(\frac{r}{a}\right) d\left(\frac{r}{a}\right) \mathrm{d}\theta. \tag{11}$$

Using the autospectral density for the unsteady axial force, the r.m.s. axial force coefficient is defined as $C_a' = G_{zz}(f)/\frac{1}{2}\rho U_\infty^2 A$. In the next section, we will present the experimental methods used to determine the unsteady wall pressures on the cylinder end-cap. Analysis of the measured cross-spectral density functions will determine the scales and functional forms of the parameters needed in equation (11).

3. EXPERIMENTAL SETUP

3.1. Wind Tunnel

Fluctuating wall pressure measurements were made on a 0·305 m long × 0·153 m diameter aluminum cylinder in a specially designed low-noise wind tunnel located in a semi-anechoic chamber. The cylinder aspect ratio was chosen to correspond to that commonly used for underwater acoustic surveillance sensors. The cylinder diameter was chosen to produce Reynolds numbers in the range of tunnel operation that would correspond to underwater acoustic sensors exposed to, due to oceanic currents in the 0·1–0·5 knot range. The cylinder was rigidly mounted to a sting attached to the mid-point of the cylinder at the rearward stagnation point. This mounting arrangement provided a finite-length cylinder with two ends, which were free of mounting-induced flow disturbances. A side-view of the wind tunnel test section is shown in Figure 2. The 11:1 contraction section of the wind tunnel leads to a 0·457 m square test-section, 1·50 m long, resulting in a tunnel blockage of 22%. In the subcritical range, Richter & Naudascher (1976) showed an increase in cylinder unsteady lift and a decrease in cylinder unsteady drag for increasing blockage ratios. Work by Blackburn (1994) showed little to no change in measured correlation lengths, obtained from spanwise surface pressure measurements, as a function of blockage ratio, for transducer separation distances less than twice the diameter. No blockage corrections were applied to the data presented here. Downstream, the test-section diffuses at a 7° angle to slow the flow, thereby minimizing acoustic radiation from the trailing edge of the open-ended exit. The cylinder was held by a 0·305 m long sting attached to a vertical steel tube with an aerodynamic cross-section.

Prior to making unsteady pressure measurements on the cylinder, both the mean, U_∞, and the fluctuating, u', velocity field in the test-section were measured using a single-component hot-wire anemometer. Mean velocity profile surveys were conducted over a plane normal to the flow direction and situated at the leading edge of the cylinder. The speeds considered were 1·83, 2·44 and 3·06 m/s, which correspond to cylinder diameter Reynolds numbers of Re = 19 200, 25 600, and 32 000, respectively. The mean velocity across the test-section was within $\pm 2{\cdot}0\%$ of that measured at the center-line. The streamwise component of turbulence intensity at the same location was less than 0·5% for all three speeds.

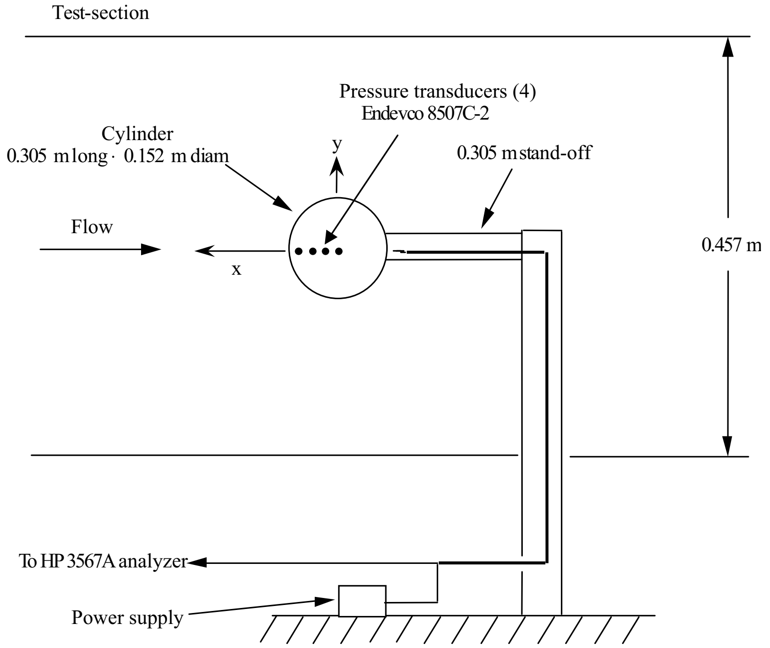

Figure 2. Side-view of wind tunnel test-section, with cylinder mounted in test position.

3.2. UNSTEADY WALL-PRESSURE MEASUREMENTS

Unsteady wall-pressure spectral measurements were made for $1 \leq f \leq 40$ Hz corresponding to Strouhal numbers, $0{\cdot}05 \leq fD/U_\infty \leq 3{\cdot}33$. Detailed results for $\mathrm{Re} = 19\,200$ and 32 000 will be presented in this paper. Results for $\mathrm{Re} = 25\,600$ will be used to formulate conclusions and to verify the scaling relationships developed. For all Reynolds numbers, a detailed map of the unsteady wall-pressure field on the cylinder end-cap was acquired. Spectral data were obtained using a Hewlett Packard (HP) 3567A dynamic signal analyzer. The analyzer was set up with 256 averages, Hanning window, 800 lines of resolution, and a 2048 line FFT. For the case of 256 averages, the normalized random error (Bendat & Piersol 2000) is $\pm 0{\cdot}0625$. This error produces spectral estimates, with 95% confidence intervals, of $\pm 12{\cdot}5\%$. The acquired data were corrected to a 1 Hz bandwidth. The wind tunnel background noise was determined from the unsteady wall-pressure measurement at the forward stagnation point of the cylinder. Prior to mounting the model in the test-section, the background noise of the tunnel was measured at all three flow speeds using the B&K microphone mounted in a slit tube. The slit tube allows measurement of the background acoustic noise in a wind stream while discriminating against boundary layer flow noise on the sensor. For $\mathrm{Re} = 32\,000$ the r.m.s. value of the background acoustic noise in the tunnel, normalized by the dynamic head, was measured to be 0·02. Measurements of the normalized r.m.s. unsteady surface pressures on the end-cap typically ranged from 0·02 to 0·26. The unsteady pressures on the end-cap of the cylinder were measured using four individual Endevco 8507C-2 piezoresistive pressure transducers. These transducers have an active sensing diameter of 0·234 cm.

The cylinder end-cap was perforated with four, 0·320 cm diameter measurement holes, and 12 0·930 cm diameter mounting holes. The measurement holes were located radially at $r = 0{\cdot}0$, 0·025, 0·051, and 0·067 m. The 12 mounting holes were used to rotate the end-cap in 30° increments. At each angular orientation, data from all four pressure transducers were acquired simultaneously. The unsteady pressure transducer in the center of the end-cap remained fixed throughout the measurement procedure. In this manner, a total of 37 independent unsteady surface pressure measurements were acquired. The 36 cross-spectral measurements from the 12 angular and three radial locations are all referenced to the transducer in the center of the end-cap. The cross-spectra between the center location and three radial locations on the opposite end-cap were also acquired.

Performing the end-cap measurements in the manner described above allows two methods of analyzing the data. The spatial nonhomogeneity of the pressure field can be determined from examination of the individual pressure measurements. Also, using the center pressure transducer as a reference, radial and circumferential correlation scales can be computed for the end-cap.

4. RESULTS

4.1. END-CAP UNSTEADY WALL-PRESSURE POWER SPECTRAL DENSITIES

The fluctuating wall pressures on the cylinder end-caps are expected to be nonhomogenous due to the locally separated flow region over the end-cap. The power spectral densities measured at discrete locations along the end-cap center-line in the streamwise x-direction are shown in Figure 3 for $\mathrm{Re} = 32\,000$ and 19 200. It is evident from Figure 3 that the magnitude of the unsteady wall pressure depends on the streamwise measurement location. The highest unsteady pressure levels at $r/a = 0{\cdot}33$ and $\theta = 180°$ may be due to the reattachment of the separated flow. Flow visualization of this phenomenon is given in

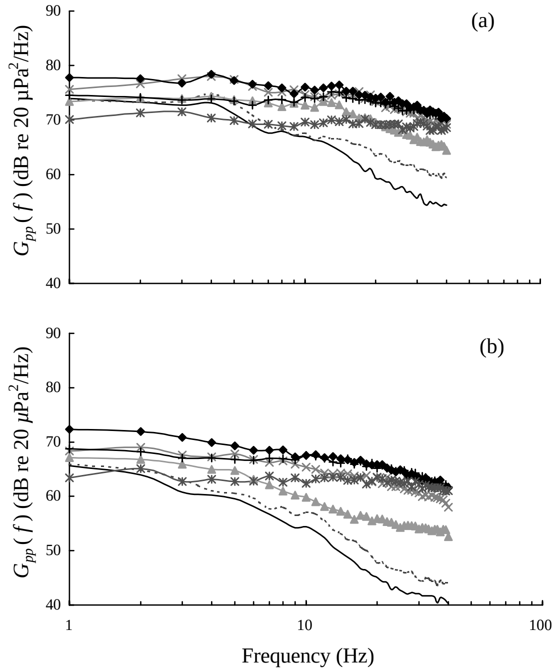

Figure 3. Circumferential variation of end-cap r.m.s. wall pressure level for a fixed radial location for (a) Re = 32 000 and (b) Re = 19 200: —— 0°, $r/a = 0{\cdot}88$; -------, 0°, $r/a = 0{\cdot}67$; ◆, 0°, $r/a = 0{\cdot}33$; ×, 0°, $r/a = 0{\cdot}0$; +, 180°, $r/a = 0{\cdot}33$, ▲, 180°, $r/a = 0{\cdot}67$; and ⁎, 180°, $r/a = 0{\cdot}88$.

McEachern & Lauchle (1995). Power spectral densities measured along a radial direction normal to the mean flow vector, $\theta = 90^\circ$, are shown in Figure 4. The unsteady pressure levels across the span of the end-cap remain relatively constant; thus, the nonhomogeneity of the pressure field appears to be primarily in the streamwise direction.

In order to facilitate the modelling of the unsteady forces on the body, a functional form of the r.m.s. value of the unsteady wall pressures on the cylinder end-cap was determined. A least-squares fit to the measured end-cap r.m.s. unsteady wall-pressure levels is shown in Figure 5. Note that the r.m.s. pressures are normalized by the dynamic head of the free stream, $q = \frac{1}{2}\rho U_\infty^2$. Only the 0–180° region of the end-cap is considered due to the symmetry of the end-cap flow about the x-direction. The symmetry of the flow was verified by comparing the r.m.s. values for the three radial locations along the y-axis at $\theta = 90^\circ$ with those at the $\theta = 270^\circ$ location. These measurements agree within the experimental accuracy of the experiments.

As observed in the data of Figure 5, the r.m.s. pressure levels are highest near the $\theta = 90-120^\circ$ locations for radial location $r/a = 0{\cdot}88$, and the $\theta = 150-180^\circ$ locations for radial locations $r/a = 0{\cdot}33$ and $0{\cdot}67$. Figure 3 shows that along the cylinder centerline the highest unsteady pressure levels are at the $\theta = 180^\circ$, $r/a = 0{\cdot}33$ location. Thus, it is likely that the high unsteady pressure levels in the region downstream of the end-cap center position, $r/a = 0{\cdot}0$, are due to the reattachment of the separated flow onto the end-cap. Figure 1 of McEachern & Lauchle (1995) shows this flow field very clearly.

The reference autospectral density, $G_{p_r p_r}(f, 0, 0)$, used in equation (10), provides the frequency content of the end-cap local wall-pressure fluctuations at a well-defined point. The variation of this spectral information over the end-cap is thus contained in the curve fitting of $B(r/a, \theta)$.

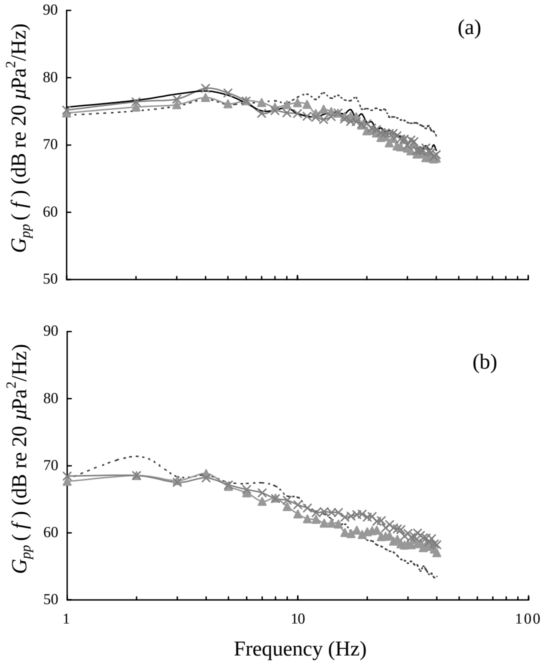

Figure 4. Spanwise variation of the unsteady wall-pressure power spectral density. (a) Re = 32 000 (b) Re = 19 200: -------, 90°, $r/a = 0{\cdot}88$; ▲, 90°, $r/a = 0{\cdot}67$; ×, 90°, $r/a = 0{\cdot}33$; and ——, 0°, $r/a = 0{\cdot}0$.

Assuming the radial and circumferential dependence of the r.m.s. pressure is separable, a second-order polynomial curve fit for the circumferential variation is

$$B(\theta) = \frac{p_{\mathrm{rms}}^{\mathrm{ref}}}{q}(f_2\theta^2 + f_3\theta + f_4). \tag{12}$$

Here, $p_{\mathrm{rms}}^{\mathrm{ref}}$ is the reference location r.m.s. pressure fluctuation, and the empirical constants f_2–f_4 are arithmetic averages of the respective coefficients determined from the data measured at all three Reynolds numbers. The radial variation of the r.m.s. pressure fluctuation is given by

$$\frac{p_{\mathrm{rms}}}{p_{\mathrm{rms}}^{\mathrm{ref}}} = \mathrm{e}^{f_1[(r/a)-1]}. \tag{13}$$

Here f_1 is the empirical constant again determined from an average over all Reynolds numbers considered. Combining equation (13) with (12) results in

$$B(r/a, \theta) = \frac{p_{\mathrm{rms}}^{\mathrm{ref}}}{q}\mathrm{e}^{f_1[r/a-1]}(f_2\theta^2 + f_2\theta + f_4), \tag{14}$$

where $f_1 = 0{\cdot}30, f_2 = -0{\cdot}18, f_3 = 0{\cdot}70$, and $f_4 = 0{\cdot}50$.

Comparisons of the predictions made with equation (14) with the experimental data of Figure 5 are shown in Figure 6. The model captures the main features of the r.m.s. wall-pressure fluctuations on the end-cap of the cylinder within the range of Reynolds numbers considered. Variations between model and data are due to the averaging of the empirical constants over all Reynolds numbers and to the selection of a second-order polynomial for $B(\theta)$.

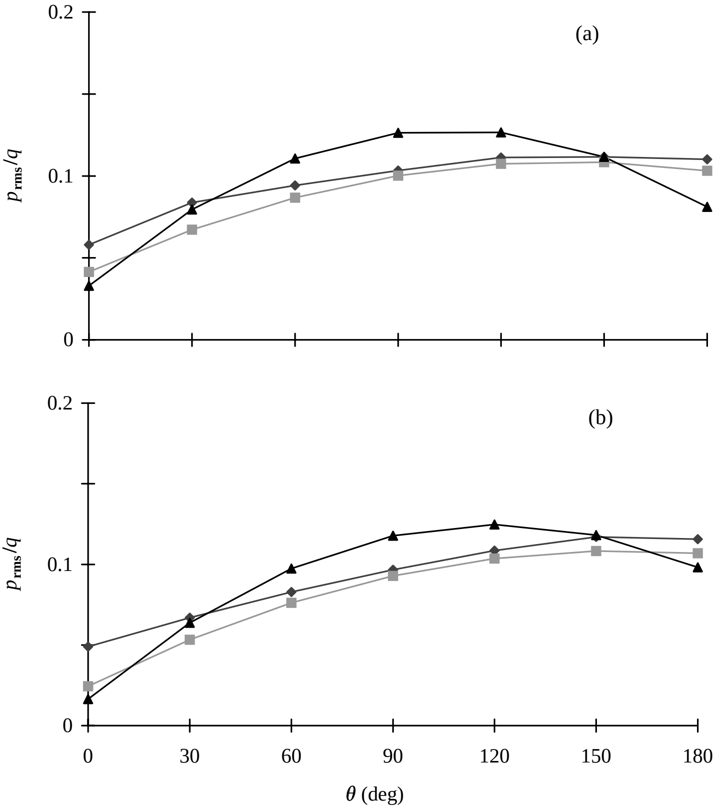

Figure 5. Circumferential variation of end-cap r.m.s. wall pressure level for three fixed radial locations for (a) $\mathrm{Re} = 32\,000$ and (b) $\mathrm{Re} = 19\,200$: ▲, $r/a = 0{\cdot}33$; ■, $r/a = 0{\cdot}67$; and ◆, $r/a = 0{\cdot}88$.

4.2. End-Cap Radial Correlation Areas

The end-cap radial correlation areas are calculated from equation (8) using the measured unsteady pressure cross-spectral data as a function of angular orientation and Strouhal number. Due to the limited number of measurement locations in the radial direction, the only reference location used for the radial cross-spectral measurements is $r = 0$. Cross-spectra were measured at discrete pairs of separation points, but the correlation length calculation requires a continuous representation of the cross-spectra as a function of separation distance. Therefore, a polynomial fit to the measured cross-spectral data is numerically integrated to produce the correlation lengths at each measured frequency and given reference location. Some frequency-to-frequency variation in the computed magnitude was observed. This is due to the relatively large spatial resolution and the relatively narrow frequency resolution of the measurements.

The radial correlation areas based on a least mean-square fit of the measured cross-spectral density functions are shown in Figure 7. Additional circumferential locations and greater detail is given in Capone (1999). For $\mathrm{St} < 0{\cdot}30$, the correlation areas are small, while they remain essentially constant from $0{\cdot}30 < \mathrm{St} < 2{\cdot}0$. The extent of the region of separated flow over the end-cap defines the largest scale eddies which exist in the flow. Below a certain cut-off frequency, in this case around $\mathrm{St} = 0{\cdot}30$, the flow cannot support structures larger than the largest eddies in the separated flow; hence, the correlation areas approach zero very rapidly for the small Strouhal numbers. These results are consistent with the results of flow

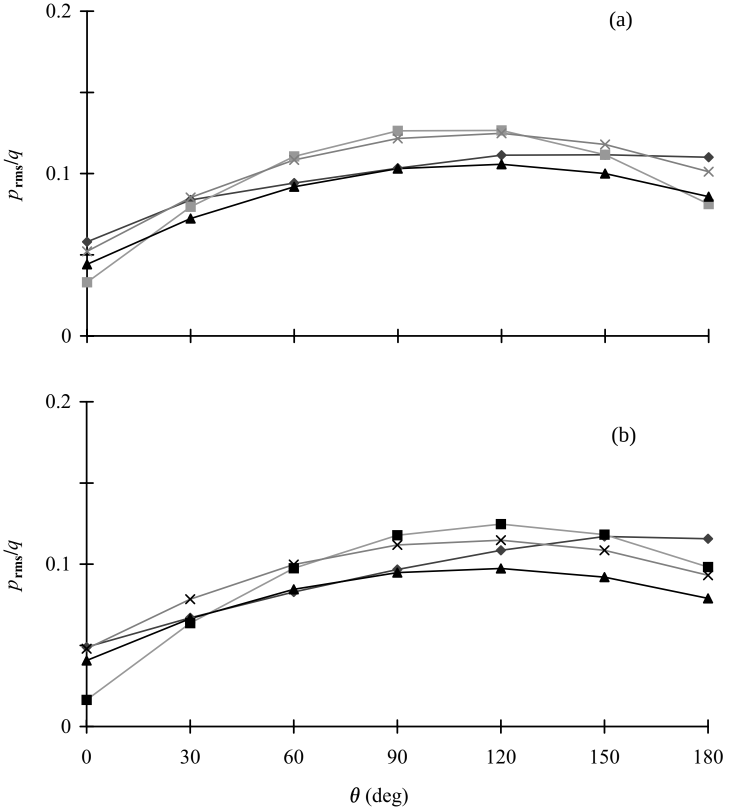

Figure 6. Comparison of the measured r.m.s. wall-pressure fluctuations on the end-cap of the cylinder with the empirical models for (a) Re = 32 000, (b) Re = 19 200: ■, $r/a = 0{\cdot}33$; ▲, $r/a = 0{\cdot}88$; ×, empirical fit, $r/a = 0{\cdot}33$; and ◆, empirical fit, $r/a = 0{\cdot}88$.

visualization, shown in Figure 8, performed by Cimbala & Lauchle (1987). Figure 8 shows a large-scale eddy with a size on the order of the cylinder diameter. Using a characteristic length of the cylinder diameter, St = 0·30, and a flow velocity of 3·05 m/s (Re = 32 000), the unsteady pressures on the end-cap should peak around 6 Hz.Figure 3(a) and 4(a) show a peak in the unsteady pressures between 4 and 5 Hz, indicating a maximum length scale slightly larger than *D*. For St > 2·0, the area decreases slightly with increasing St. This gradual decay is indicative of shorter characteristic length scales. In general, larger, low-frequency flow structures maintain their identity over a given separation distance better than higher-frequency, smaller-scale eddies. This results in a weak decay of the radial correlation areas with increasing Strouhal number. The magnitudes of the radial correlation areas show little variation over the range of Reynolds numbers tested. This is consistent with the results of West & Apelt (1997), who found no measurable variation in the spanwise cross-correlation of pressure for a cylinder subjected to low turbulence flow in the subcritical range.

The Strouhal-number dependence of the radial correlation areas is modelled using an equation similar to that for a Rayleigh probability distribution function. The correlation area is represented by

$$\frac{\Lambda_r(\mathrm{St})}{a^2} = \frac{h_1 \mathrm{St}}{h_2^2} \exp\left[\frac{-\mathrm{St}^{0.35}}{(2h_2^2)}\right], \tag{15}$$

where h_1 and h_2 are empirical constants.

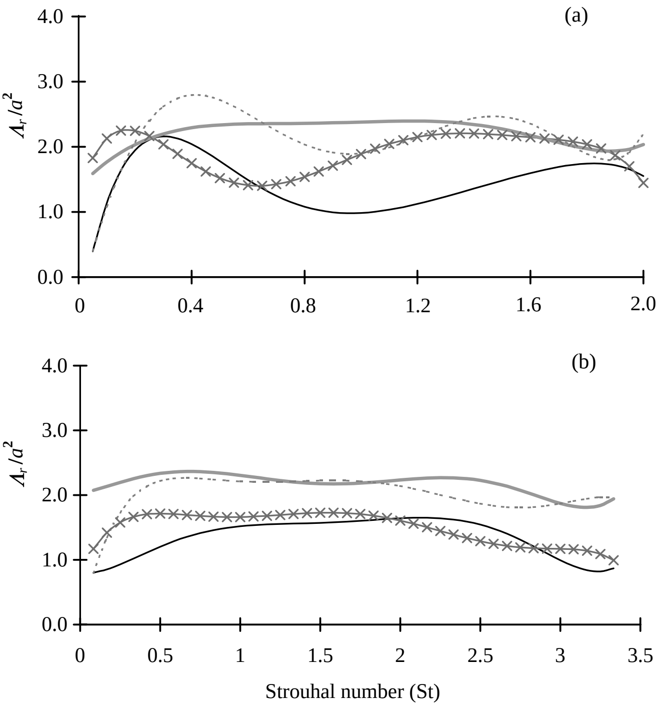

Figure 7. Radial correlation areas for angular locations $\theta = 0°$, 60°, 120°, and 180°; (a) Re = 32 000, (b) Re = 19 200: ——, $\theta = 0°$; ×, $\theta = 60°$; --------, $\theta = 120°$; and ——, $\theta = 180°$.

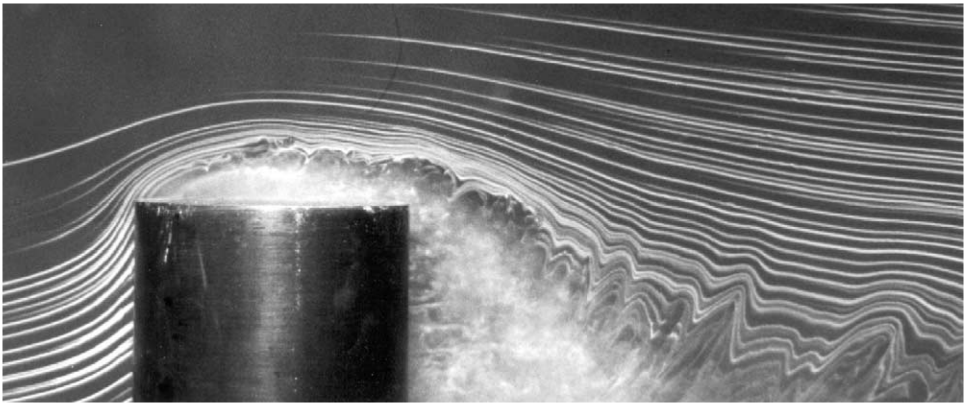

Figure 8. Smoke wire flow visualization of the flow over the end-cap of a right circular cylinder at Re = 33 000 (after Cimbala & Lauchle (1987)).

The variation of the radial correlation area with circumferential location is determined from cross plots of the data as a function of θ at constant St. Analysis of the results given in Figure 7 shows that the correlation areas are the smallest at $\theta = 0$ and 60°, peak at 120°, and then decrease slightly at 180°. The increase in correlation areas around the 120° location is presumed to be a result of the proximity to the end-cap separated flow reattachment location. For example, the approximate downstream location of reattachment along the x-axis is $\theta = 180°$, $r/a = 0{\cdot}33$. Assuming that the reattachment line is parallel to the y-axis, this corresponds to an off x-axis location of $r/a = 0{\cdot}66$ for $\theta = 120°$. For separated flow over a backward facing step, Farabee (1986), found streamwise coherence values aft of the flow reattachment point to be significantly higher than those for the nonseparated, equilibrium flow. Given this, the increase in correlation areas around the 120° location makes physical sense. Assuming the correlation area peaks at 120°, and it has approximately the same value at 60 and 180°, the empirical curve fit for the circumferential variation of the end-cap correlation area is given by

$$\frac{\Lambda_r(\theta)}{\Lambda_{r\mathrm{ref}}} = 1 + 0{\cdot}5\sin\left(\frac{3\theta}{4}\right), \tag{16}$$

where $\Lambda_{r\mathrm{ref}}$ is the reference correlation area determined at $\theta = 0°$.

Combining equations (15) and (16) yields the radial correlation area as a function of Strouhal number and angular location

$$\frac{\Lambda_r(\mathrm{St},\theta)}{a^2} = \frac{h_1\mathrm{St}}{h_2^2}\exp\left[\frac{-\mathrm{St}^{0.35}}{(2h_2^2)}\right]\left(1 + 0{\cdot}5\sin\left(\frac{3\theta}{4}\right)\right)\Lambda_{r\mathrm{ref}}, \tag{17}$$

where $h_1 = 7{\cdot}5$, and $h_2 = 0{\cdot}4$.

Predictions using equation (17) are compared to the radial length-scales for $\theta = 0$ and 120° at Re = 32 000 and 19 200 in Figure 9.

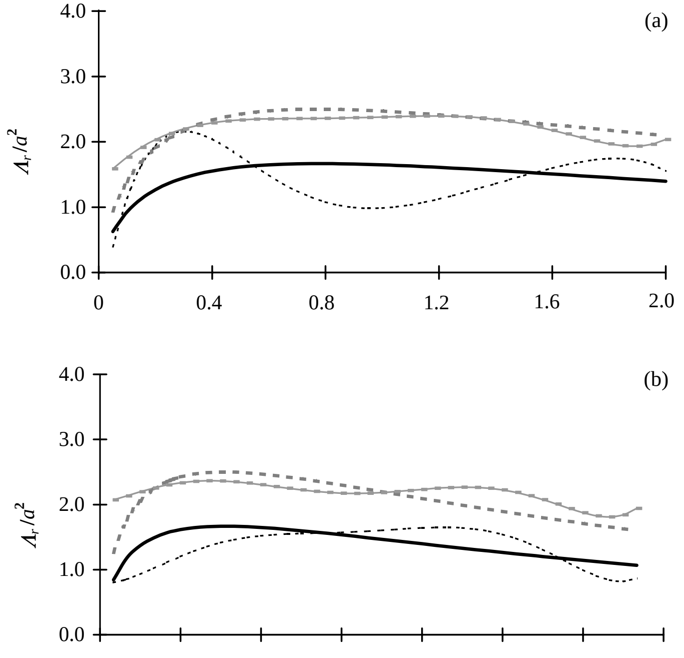

Figure 9. Empirical fit of the end-cap radial correlation areas as a function of Strouhal number and circumferential location compared to measured data with a reference location of $\theta = 0°$; (a) Re = 32 000, (b) Re = 19 200: -------, $\theta = 0°$; ——, fit, 0°; --------, $\theta = 120°$; and - - - - -, fit, 120°.

4.3. END-CAP CIRCUMFERENTIAL CORRELATION LENGTHS

The end-cap circumferential correlation lengths, equation (9), were also calculated from the measured unsteady pressure cross-spectral data. These length-scales are computed as a function of radial location and frequency, and a suggested model form is derived.

The least-squares fit to the experimentally determined circumferential length-scales for the single reference location of $\theta = 0^\circ$ are shown in Figure 10. The Strouhal number dependence of these scales is similar to that of the radial correlation areas. After the peak near St = 0·21, the correlation lengths decay slowly a with increasing Strouhal number. The dependence of Λ_θ on Strouhal number is obtained using the equation:

$$\Lambda_\theta(\mathrm{St}) = \frac{h_3\mathrm{St}}{h_4^2}\exp\left[\frac{-\mathrm{St}^{0.42}}{(2h_4^2)}\right], \tag{18}$$

where h_1 and h_2 are empirical constants.

The circumferential correlation lengths are highest for $r/a = 0{\cdot}33$ and decrease with increasing radial position. This decrease for increasing radial location is not unexpected based upon the definition of Λ_θ, equation (9). The length-scales are computed as a function of $\Delta\theta$ for all radial locations. Although the angular separation is constant for each radial location, the physical separation between measurement points increases with increasing radial location. Therefore, for a given $\Delta\theta$ the magnitude of the cross-spectral density function measured at $r/a = 0{\cdot}88$ is typically lower than that measured at smaller values of r/a.

The variation of the circumferential correlation lengths with radial location is determined from cross plots of the length-scale data as a function of r/a at constant St. Combining the radial dependence of the length-scales with the Strouhal dependence

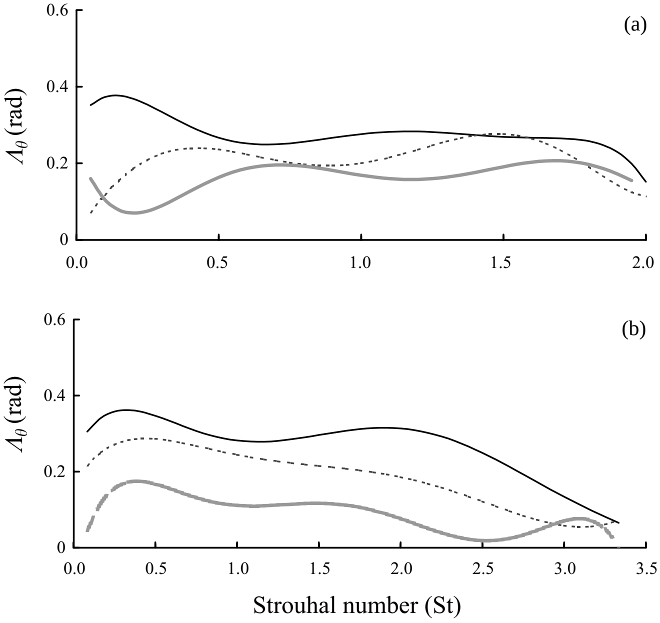

Figure 10. Circumferential length-scales at Re = 32 000 and 19 200 for radial locations of $r/a = 0{\cdot}33$, 0·67, and 0·88, and a reference location of $\theta = 0^\circ$; (a) Re = 32 000, (b) Re = 19 200: ——, $r/a = 0{\cdot}33$; -------, $r/a = 0{\cdot}67$; and -------, $r/a = 0{\cdot}88$.

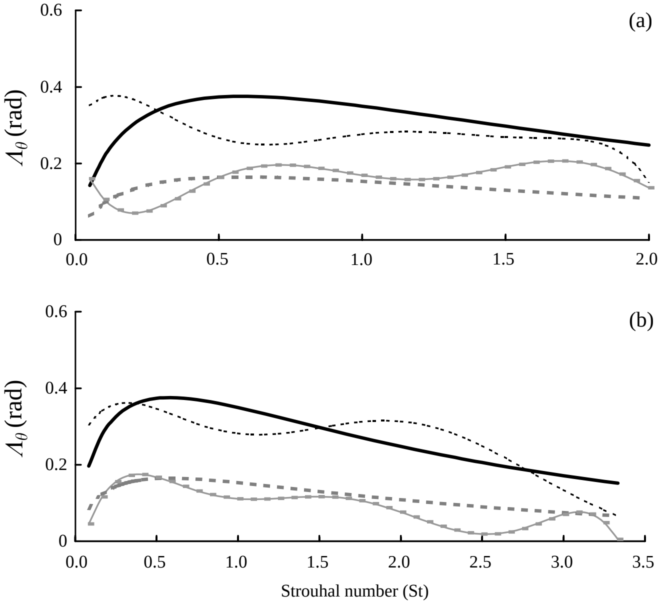

Figure 11. Empirical fit of the circumferential correlation lengths as a function of Strouhal number and radial location compared to those measured; (a) Re = 32 000, (b) Re = 19 200: -------, $r/a = 0{\cdot}33$; ········, empirical fit, $r/a = 0{\cdot}33$; —— $r/a = 0{\cdot}88$; and - - - -, empirical fit, $r/a = 0{\cdot}88$.

provides the final form for the end-cap circumferential length-scales:

$$\Lambda_\theta(\mathrm{St}, r/a) = \frac{h_3\mathrm{St}}{h_4^2}\exp\left[\frac{-\mathrm{St}^{0.42}}{(2h_4^2)}\right] h_5 \exp\left[h_6(r/a - 1)\right], \qquad (19)$$

where $h_3 = 1{\cdot}05$, $h_4 = 0{\cdot}45$, $h_5 = 0{\cdot}37$ and $h_6 = 1{\cdot}5$.

Predictions based on equation (19) are compared to the measured circumferential lengthscales in Figure 11.

5. UNSTEADY FORCE PREDICTIONS

The unsteady axial force spectrum is calculated using equation (11) together with the model results from equations (14), (17) and (19). Figure 12 shows the coherence function measured between pressure sensors located at $r/a = 0{\cdot}0$ and on the two opposing end-caps. Coherence measurements between the $r/a = 0{\cdot}0$ location on the first end-cap and $\theta = 90^\circ$, $r/a = 0{\cdot}67$, and 0·88 on the second, show a similar low coherence level. Based on these low coherence values measured between the opposing end-caps, the total unsteady axial force acting on the cylinder is calculated by assuming the forces on each end can be summed incoherently.

The calculated spectra are presented in Figure 13 as dimensionless fluctuating force spectrum, where A is the area of the cylinder end-cap. Note that the use of the reference autospectral density, $G_{p_r p_r}(f, r_r, \theta_r)$, in equation (10) results in a predicted unsteady force spectrum with a character similar to that of the reference wall-pressure spectrum. The data are seen to collapse well using the inertial force and time scales of the flow for nondimensionalization. This is consistent with the results of McEachern & Lauchle (1995) for flow noise on operational sensors.

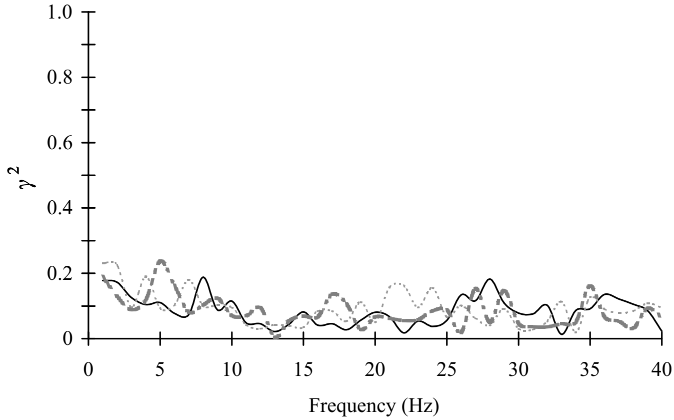

Figure 12. Coherence function measured between pressure transducers mounted at $r/a = 0{\cdot}0$ on opposing end-caps: ——, Re = 32 000; - - - - - - -, Re = 25 600; - - - -, and Re = 19 200.

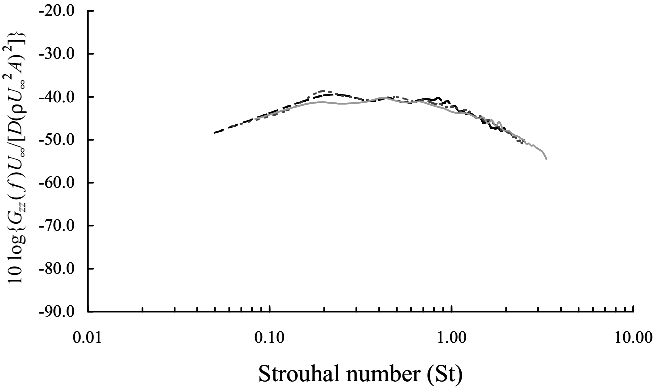

Figure 13. Unsteady axial force predictions for Re = 32 000, 25 600, and 19 200: - - - -, Re = 32 000; - - - - - - -, Re = 25 600; and ——, Re = 19 200.

Currently, no published data are available for validation of the predicted unsteady axial force. For future comparison purposes, the r.m.s. unsteady axial force coefficient, computed for the three Reynolds numbers tested, 32 000, 25 000, and 19 200 are 0·020, 0·021, and 0·019, respectively. Also, a comparison to the power summation of the absolute levels of the unsteady lift and drag on the same finite cylinder, Capone & Lauchle (2000), is shown in Figure 14. Absolute levels are compared here, because different reference areas are required for normalization of the unsteady forces for the two cases. Above 10 Hz, the unsteady axial force levels are larger than those of the combined unsteady lift and drag. Below 10 Hz, the unsteady lift and drag are the dominant unsteady force. Converting to a Strouhal number scale, this cross-over frequency corresponds to St = 0·83. Even in the absence of a clear coherent vortex-shedding process from a 3-D cylinder, the predominant energy in the fluctuating lift and drag fluctuations is concentrated in a broad spectral hump centered at the Strouhal shedding frequency. This is in marked contrast to the discrete tone observed in the force spectra of 2-D cylinders. Our results further suggest that the separated flow region over the end-caps of the 3-D cylinder results in a relatively broadband axial forcing function with no apparent connection to the cylinder shedding frequency.

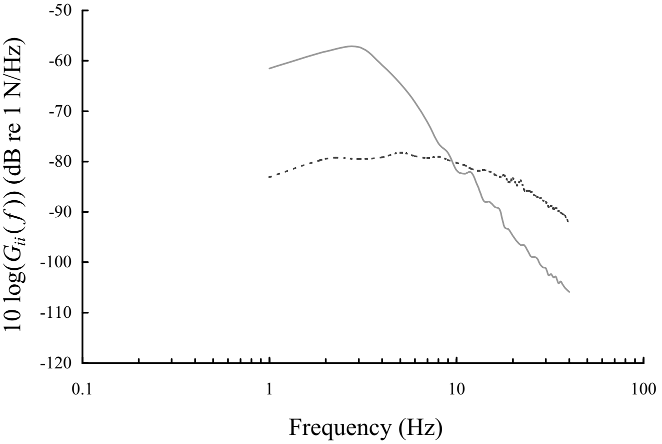

Figure 14. Comparison of the predicted unsteady axial force with the combined unsteady lift and drag forces at Re = 19 200: --------, unsteady axial force, $i = z$; and ——, unsteady lift and drag, $i(x + y)$.

6. CONCLUSIONS

Measurements of the unsteady pressure field on the cylinder end-cap show the highest r.m.s. wall-pressure levels to be in the 90–120° locations. The high r.m.s. pressures in these locations are due to flow reattachment across the span of the end-cap, and to the proximity to the separation point on the cylinder body. In view of the unsteady lift and drag reported by Capone & Lauchle (2000), the unsteady wall-pressure power spectral data on the end-cap show much different frequency character than wall-pressure spectra measured on cylindrical surfaces. Due to the strong contribution from coherent vortex shedding, the energy in the wall-pressure fluctuations measured on the cylindrical surfaces is concentrated in a Strouhal number range below St = 0·5, while energy in the wall pressures measured on the end-cap is much more evenly distributed over Strouhal number.

The radial correlation areas and circumferential length-scales on the end-cap do not decay as rapidly with increasing Strouhal number, as do the axial and circumferential length-scales on the cylindrical surface. This is due to the low-frequency, large eddy structures present in the end-cap flow. The radial correlation area on the end-cap is a maximum at the 120° location. The circumferential length-scale decreases with increasing radial location. This, however, is an artifact of the experiment due to the variation of angular separation distance with changing radial location. For St < 0·8, the predicted unsteady axial forces are considerably smaller than the unsteady lift or drag forces (as much as 20 dB). Even in the absence of an axially coherent discrete vortex-shedding process, the majority of the energy in the fluctuating lift and drag spectra is concentrated about the Strouhal shedding frequency. The axial force spectra are much more broadband, indicating that the shedding from the cylindrical surface has little effect on the unsteady axial force fluctuations.

ACKNOWLEDGEMENTS

The work reported here has been supported by ONR Code 321SS, Scott Littlefield, under grant number N00014-96-1-0005.

REFERENCES

BABAN, F., SO, R. M. C. & OTUGEN, M. V. 1989 Unsteady forces on circular cylinders in a cross-flow. *Experiments in Fluids* **7,** 293–302.

BENDAT, J. S. & PIERSOL, A. G. 2000 *Random Data Analysis and Measurement Procedures*, 3rd edition. New York: John Wiley and Sons.

BLACKBURN, H. M. 1994 Effect of blockage on spanwise correlation in a circular cylinder wake. *Experiments in Fluids* **1,** 134–136

CAPONE, D. E. 1999 Modeling the unsteady forces on a finite-length circular cylinder in cross-flow. Ph. D. Thesis, The Pennsylvania State University, University Park, PA, USA

CAPONE, D. E. & LAUCHLE, G. C. 2000 Modeling the unsteady lift and drag on a finite-length circular cylinder in cross-flow. *Journal of Fluids and Structures* **14,** 799–817.

CIMBALA, J. & LAUCHLE, G. C. 1987 Flow visualization study of the tip region of a cylinder in cross flow. Applied Research Laboratory Technical Memorandum, File Number 87–77.

CRIGHTON, D. C., DOWLING, A. P., FFOWCS WILLIAMS, J. E., HECKL, M. & LEPPINGTON, F. G. 1992 *Modern Methods in Analytical Acoustics Lecture Notes*. London: Springer-Verlag.

FARABEE, T. M. 1986 An experimental investigation of wall pressure fluctuations beneath non-equilibrium turbulent flows. Report No. DTNSRDC-86/407, David W. Taylor Naval Ship Research and Development Center.

FARIVAR, D. J. 1981 Turbulent flow around cylinders of finite length. *AIAA Journal* **19,** 275–281.

FINGER, R. A., ABBAGNARO, L. A. & BAUER, B. B. 1979 Measurements of low-velocity flow noise on pressure gradient hydrophones. *Journal of the Acoustical Society of America* **65,** 1407–1412.

KEEFE, R. T. 1961 An investigation of the fluctuating forces acting on a stationary circular cylinder in a subsonic stream and of the associated sound field. UTIA Report No. 76, Institute of Aerophysics, University of Toronto.

MCEACHERN, J. F. 1993 The effect of body geometry on the flow noise of cylinders in cross flow. Ph. D. Thesis, The Pennsylvania State University, University Park, PA, USA

MCEACHERN, J. F. & LAUCHLE, G. C. 1995 Flow-induced noise on a bluff body. *Journal of the Acoustical Society of America* **97,** 947–953.

RIBEIRO, J. L. D. 1992 Fluctuating lift and its spanwise correlation on a circular cylinder in a smooth and in a turbulent flow: a critical review. *Journal of Wind Engineering and Industrial Aerodynamics* **40,** 179–198.

RICHTER, A. & NAUDASCHER, E. 1976 Fluctuating forces on a rigid circular cylinder in confined flow. *Journal of Fluid Mechanics* **78,** 561–576.

WEST, G. S. & APELT, C. J. 1997 Fluctuating lift and drag forces on finite lengths of a circular cylinder in the subcritical Reynolds number range. *Journal of Fluids and Structures* **11,** 135–158.